APL Photonics

Controlling dispersion in multifunctional metasurfaces

Cite as: APL Photonics **5**, 056107 (2020); https://doi.org/10.1063/1.5142637
Submitted: 15 December 2019 . Accepted: 24 April 2020 . Published Online: 22 May 2020

Jared Sisler, Wei Ting Chen, Alexander Y. Zhu, and Federico Capasso

COLLECTIONS

This paper was selected as Featured

View Online Export Citation CrossMark

APL Photonics The Future Luminary Award
Journal Impact Factor 4.383
LEARN MORE!

© 2020 Author(s).

Controlling dispersion in multifunctional metasurfaces

Cite as: APL Photon. 5, 056107 (2020); doi: 10.1063/1.5142637
Submitted: 15 December 2019 • Accepted: 24 April 2020 •
Published Online: 22 May 2020

View Online Export Citation CrossMark

Jared Sisler,[1,2] Wei Ting Chen,[1,a)] Alexander Y. Zhu,[1] and Federico Capasso[1,a)]

AFFILIATIONS

[1] Harvard John A. Paulson School of Engineering and Applied Sciences, Harvard University, Cambridge, Massachusetts 02138, USA
[2] University of Waterloo, Waterloo, Ontario N2L 3G1, Canada

[a)] Authors to whom correspondence should be addressed: weitingchen@seas.harvard.edu and capasso@seas.harvard.edu

ABSTRACT

Metasurfaces can be designed to exhibit different functionalities with incident wavelength, polarization, or angles through appropriate choice and design of the constituent nanostructures. As a proof-of-concept, we design and simulate three multifunctional metalenses with vastly different focal lengths at blue and red wavelengths to show that the wavelength dependence of focal length shift can be engineered to exhibit achromatic, refractive, or diffractive behavior. In addition, we design a metalens capable of achromatically focusing an incident plane wave to a spot and a vortex at red and blue wavelengths, respectively. These metalenses are designed with coupled subwavelength-scale dielectric TiO_2 nanostructures. Our method illustrates a more general design strategy for multifunctional metasurfaces by considering phase and group delay profiles with applications in imaging, spectroscopy, and wearable optical devices.

© *2020 Author(s). All article content, except where otherwise noted, is licensed under a Creative Commons Attribution (CC BY) license (http://creativecommons.org/licenses/by/4.0/).* https://doi.org/10.1063/1.5142637

INTRODUCTION

Metasurfaces consist of subwavelength spaced nanostructures to achieve precise control over the phase, amplitude, and polarization of light.[1,2] By tailoring the geometric shapes of these nanostructures, it has been demonstrated that a single metasurface can exhibit multiple distinct functions.[3,4] For instance, it has recently been shown that a metasurface hologram can generate different images in reflection and transmission.[5] A metasurface could also exhibit polarization-,[6–11] wavelength-,[12–15] or incident angle-dependent functionality.[16–20] This leads to numerous potential applications where information can be multiplexed with little to no increase in the spatial footprint of the device. Likewise, a metasurface lens (metalens) with multiple functions such as different focal lengths at different wavelengths, which is a desired feature for spectroscopies, has been recently demonstrated in the near-infrared and visible spectra.[21–24] Here, we report how dispersion can be controlled for these multifunctional metasurfaces and that these multiple functions of a metasurface can even include different dispersions. As a proof-of-concept, we design and simulate metalenses with vastly different focal lengths in the blue and red regions of the visible spectrum. Importantly, the dispersive behavior of these focal spots (i.e., how the focal spots move with wavelength) can be engineered to exhibit achromatic, refractive, or diffractive behavior. Additionally, beam shaping as a function of wavelength is engineered to achieve achromatic focusing of an incident beam of blue and red wavelengths to a vortex and an Airy disk, respectively. Our technique relies on dispersion engineering using coupled subwavelength nanofins and does not involve any form of spatial multiplexing. This could prove useful for a variety of applications involving pump–probe spectroscopy or fluorescence/photoluminescence microscopy and paves the way for novel optical components in the design of modern objectives and high-end optical systems.

Previous demonstrations of dispersion-engineered metalenses have often focused on reducing the focal length shift across wide, continuous bandwidths.[25–32] The versatility of our new approach allows for one device to exhibit many combinations of focal length shifts in different wavelength regions. We first designed metalenses to focus light with λ = 490 nm and λ = 660 nm at two distinct focal lengths. The focal length shifts for neighboring wavelengths (450–530 nm and 620–700 nm) were tuned by tailoring the local

© Author(s) 2020

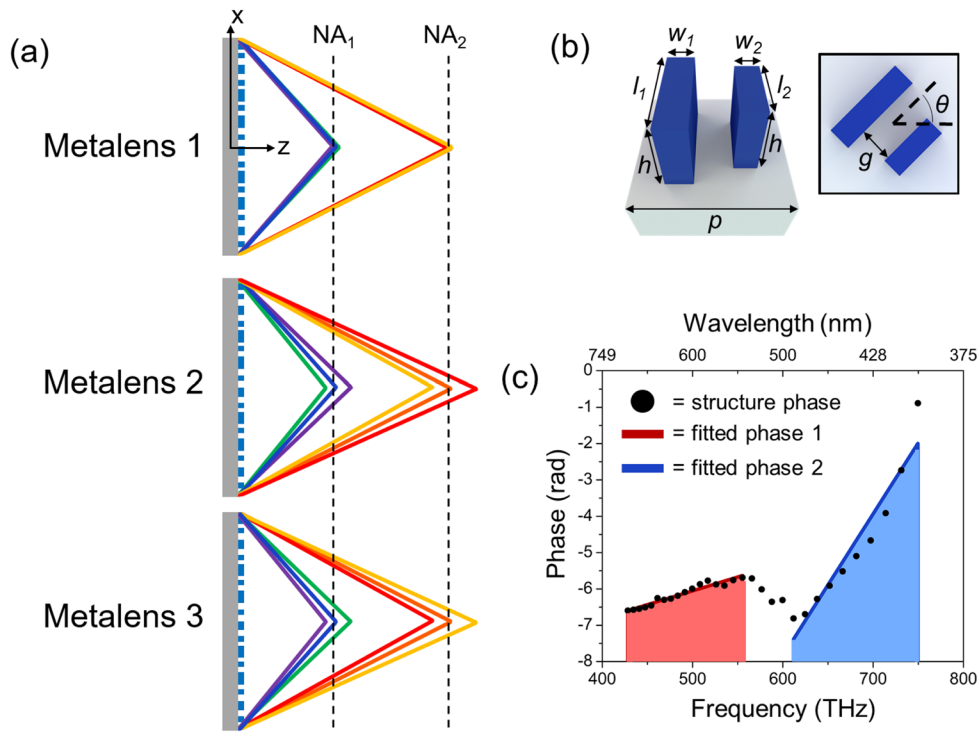

FIG. 1. Multifunctional metasurfaces. (a) Discrete bandwidth regions (450–530 nm and 620–700 nm) in the visible spectrum are focused with different numerical apertures and focal lengths. Metalens 1 employs achromatic focusing in both bandwidths, while Metalenses 2 and 3 display opposing refractive and diffractive focal length shifts with wavelength in each bandwidth. These dual focal length metalenses have a 20 μm diameter, NA_1 = 0.2 at λ_{d1} = 490 nm, and NA_2 = 0.1 at λ_{d2} = 660 nm. (b) The geometry of the metalens building block. The metalens elements were composed of TiO_2 with a constant height, h = 600 nm, and were spaced equally in the x- and y-directions with a period, p = 400 nm. The other labeled dimensions were independently adjusted at each lens coordinate to match the required phase and group delay terms. (c) Simulated and fitted phase for a single metalens element with dimensions l_1 = 270 nm, w_1 = 50 nm, l_2 = 110 nm, w_2 = 150 nm, and g = 60 nm. The black circles represent the metalens element's phase calculated from a FDTD simulation. The red and blue curves show linear fits of the phase in separate frequency regions.

dispersion. Figure 1(a) illustrates three metalenses that were designed to demonstrate the capabilities of our approach. Metalens 1 exhibits achromatic focusing around both 490 nm and 660 nm. Metalens 2 shows a diffractive focal length shift around 490 nm and a refractive focal length shift around 660 nm, while Metalens 3 shows the reverse (refractive focal length shift at 490 nm and diffractive at 660 nm). Refractive and diffractive focal length shifts refer to focusing longer wavelengths further and closer to the metalens, respectively.

PRINCIPLE AND DESIGN

In order to achieve devices with the dual functionalities described above, the individual nanostructures placed across the metalens must simultaneously exhibit two distinct phase and group delay profiles at the design wavelengths. The general metalens element used to achieve this consists of two closely spaced TiO_2 nanofins, enabling a coupled mode for better dispersion control,[33,34] as shown in Fig. 1(b). The spacing of metalens elements in each axis, p, and the height of pillars, h, were kept constant at 400 nm and 600 nm, respectively. All other values (w_1, l_1, w_2, l_2, g, θ) were adjusted to achieve the required phase and dispersion values at each metalens coordinate. Figure 1(c) shows simulated phase values (black circles) for an element. The obtained phase was fitted with two linear functions for two different bandwidths: the blue curve was fit from 400 nm to 490 nm, and the red curve was fit from 550 nm to 700 nm. As is clearly visible in Fig. 1(c), the first derivatives with respect to frequency (group delay) of these fit lines are very different. This means that this element exhibits different dispersion in the bandwidths of interest and can, therefore, be employed to achieve the functionalities outlined in Fig. 1(a).

Our methods of dispersion engineering are based on the Taylor expansion of a spatially dependent and frequency-dependent phase profile around a center or "design" angular frequency, ω_d,[26,27]

$$\varphi(r,\omega) = \varphi(r,\omega_d) + \left.\frac{\partial\varphi}{\partial\omega}\right|_{\omega=\omega_d}(\omega-\omega_d) + \cdots, \tag{1}$$

where r and ω represent the radial coordinate across the metalens and the angular frequency, respectively. To create a metalens with different dispersion characteristics in separate bandwidths, a metalens phase function with two separate dispersion characteristics can

© Author(s) 2020

be written as follows:

$$\varphi_1(r,\omega) = -\frac{\omega}{c}\left[\sqrt{r^2+f_1^2}-f_1\right] \text{ for } \frac{2\pi c}{\lambda_{530\text{nm}}} \le \omega \le \frac{2\pi c}{\lambda_{450\text{nm}}}, \quad (2)$$

$$\varphi_2(r,\omega) = -\frac{\omega}{c}\left[\sqrt{r^2+f_2^2}-f_2\right] \text{ for } \frac{2\pi c}{\lambda_{700\text{nm}}} \le \omega \le \frac{2\pi c}{\lambda_{620\text{nm}}}, \quad (3)$$

where focal lengths, f_1 and f_2, are a function of frequency and follow a general equation:

$$f(\omega) = f_d\left(\frac{\omega}{\omega_d}\right)^n. \quad (4)$$

In the equations mentioned above, the two bandwidths of interest span from 450–530 nm and 620–700 nm with the designed center wavelengths of 490 nm and 660 nm. For each design bandwidth, f_d corresponds to the focal length at the design frequency, and n is a parameter used to describe how the focal spot moves with wavelength. For the purpose of our demonstrations, we chose n = −1, n = 0, and n = 1 to represent refractive, achromatic, and diffractive focusing, respectively. Metalens 1 displays achromatic focusing in both design bandwidths, which results in a constant focal length with respect to frequency in each bandwidth. Metalens 2 exhibits a diffractive focal length shift around λ_{d1} = 490 nm and a refractive focal length shift around λ_{d2} = 660 nm, $(n_1, n_2) = (1, -1)$, while Metalens 3 has the opposite behavior and $(n_1, n_2) = (-1, 1)$. Note that since we performed a Taylor expansion, the first order derivatives of Eqs. (2) and (3) give the targeted group delay profiles. This means that a nanofin element placed at a given metalens coordinate must simultaneously satisfy four target values,

$$\left(\varphi_1(\omega_1), \quad \varphi_2(\omega_2), \quad \left.\frac{\partial\varphi_1}{\partial\omega}\right|_{\omega_1}, \quad \left.\frac{\partial\varphi_2}{\partial\omega}\right|_{\omega_2}\right), \quad (5)$$

where ω_1 and ω_2 are frequencies corresponding to the design wavelengths of 490 nm and 660 nm, respectively. This method can, in principle, be generalized for more than the two functionalities shown here. We only consider the group delay since the required bandwidth of operation is much smaller compared to previous works.[26,27,35,36] Note that, in Eqs. (2) and (3), there is a designed bandwidth gap to allow the metalens to switch from short to long focal lengths. If one wants to reduce this gap, it is necessary to design nanostructures with sharp phase variations, which can be realized through the use of a guided mode, Fabry–Perot or Mie resonances,[37–39] or interference of high order propagation waveguide modes.[40,41]

In order to realize the metalenses shown in Fig. 1(a), we first created a "library" of metalens elements consisting of the TiO_2 nanostructures depicted in Fig. 1(b). Finite-difference time-domain (FDTD) simulations were performed for 20 nm increments of each geometric variable in Fig. 1(b) to obtain far-field phase spectra of right-handed circular polarization for wavelengths in the range 400–700 nm under left-handed circularly polarized incident light. The refractive index of TiO_2 used in simulation was taken from ellipsometry measurement results.[42] The rotation angle of the metalens element, θ, was kept constant at 0° during simulation as the phase at all other angles can be predicted from the Pancharatnam–Berry phase.[43,44] After simulating each metalens element, we obtained the values of phase and group delay at the design wavelengths 490 nm and 660 nm for all elements. Each element, therefore, has its corresponding set of phase and group delay values as follows:

$$\left(\phi_1(\omega_1), \quad \phi_2(\omega_2), \quad \left.\frac{\partial\phi_1}{\partial\omega}\right|_{\omega_1}, \quad \left.\frac{\partial\phi_2}{\partial\omega}\right|_{\omega_2}\right). \quad (6)$$

To visualize the library, the left and right panels of Fig. 2(a) plot the phase for all simulated elements as blue circles, with the phase at 490 nm (ϕ_1) on the x-axis and the phase at 660 nm (ϕ_2) on the y-axis. In a similar fashion, the left and right panels of Fig. 2(b) plot the group delay for all simulated elements as blue circles, with the group delay at 490 nm on the x-axis and the group delay at 660 nm on the y-axis. Since the plots in Fig. 2(a) show the first two phase values from Eq. (6) and the plots in Fig. 2(b) show the two group delay values from Eq. (6), each blue circle in Fig. 2(a) has a "twin" circle in Fig. 2(b) that corresponds to the same library element. A further discussion of the spread of library points in these two figures is provided in the supplementary material, Fig. S1. In order to implement our designed metalenses, we compared the phase and group delay values for each library element [Eq. (6)] to those of the target obtained from Eq. (5) to select the best element for each lens position. The overlaid black dots in Figs. 2(a) and 2(b) show the target phase and group delay at every metalens coordinate to achieve the functionality of Metalens 1. To implement Metalens 1, one could choose the library element (blue circle) that has the shortest sum of distances to a given target point (black dot) in Figs. 2(a) and 2(b) and then place it at the corresponding lens coordinate. This technique, however, is limited by the match between the library [Eq. (5)] and metalens requirements [Eq. (6)] as most of the black dots are far from blue circles in Fig. 2(a). To increase our available degrees of freedom, we made use of the Pancharatnam–Berry phase,[43,44] which improved our library's phase coverage at the two design wavelengths of interest. By adjusting the rotation of a metalens element, the phase at all wavelengths will be shifted linearly, thus leaving the group delay unaffected. Since rotation will change the phase at 490 nm and 660 nm equally, it will shift a given blue point on Fig. 2(a) along a line with a slope equal to 1. Equally speaking, this means that each black "target point" can be extended to a "target line." The 45° slanted red line shown on the right panel of Fig. 2(a) displays the target line for a given target point. Now, any library element that lies close to this red line, under appropriate rotation, can realize the target phase indicated by the black dot. As a result, we have more library elements available to better fulfill group delay requirements [Fig. 2(b)]. As an example to elaborate upon the process of satisfying phase and group delay requirements, the right panels of Figs. 2(a) and 2(b) plot a black dot, purple triangle, and green square over the available library points. The purple triangle and green square represent two candidate elements that lie equally close to the target red line, which corresponds to the target black point. However, when the points are viewed in group delay space [see Fig. 2(b)], the green square is closer to the target point and is a better choice. We wrote a particle-swarm optimization algorithm to perform this selection process and obtain suitable nanofins at each position on our metalenses. Figures 2(c) and 2(d) show the comparison of target and realized phase and group delay profiles for Metalens 1 at each design wavelength. Note that the strength of our approach in using these anisotropic metalens elements lies primarily on the fact that the phase and group delay are decoupled. Under circular polarization incidence, the phase can be tuned by

© Author(s) 2020

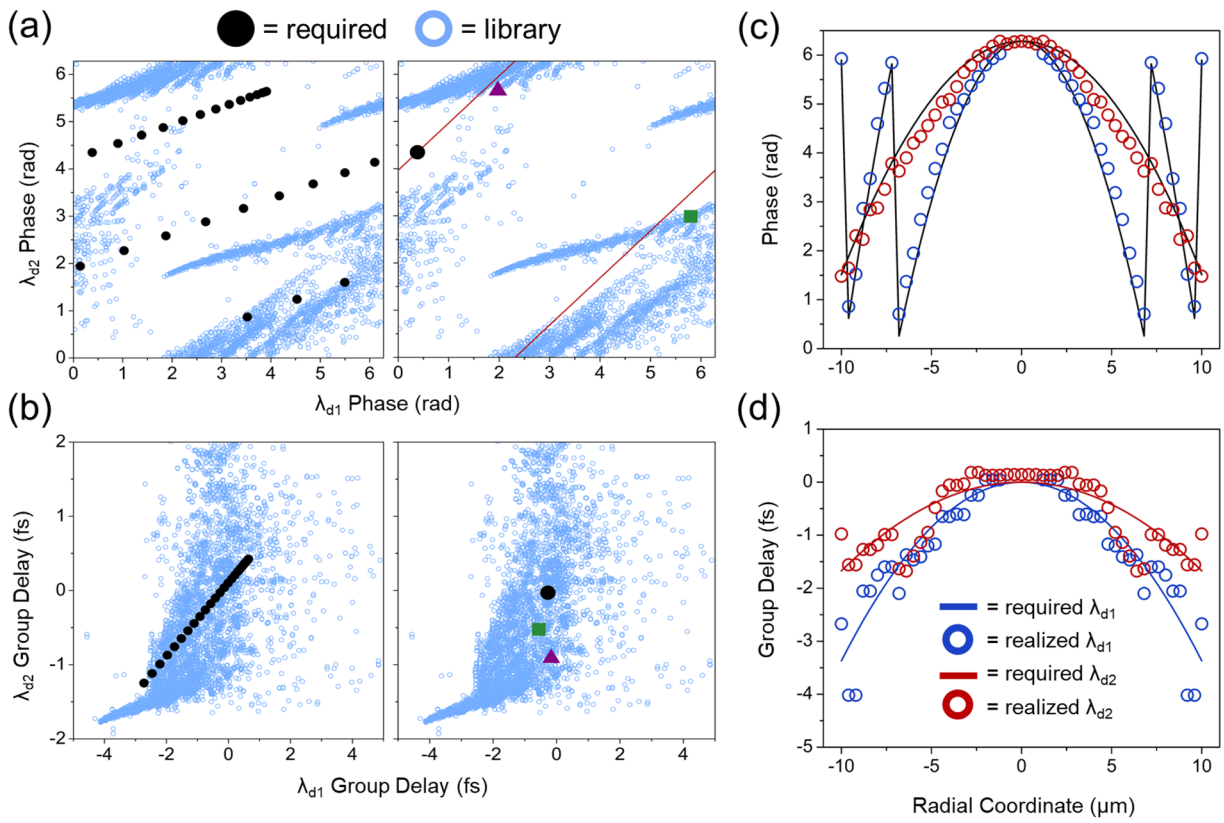

FIG. 2. Design of multifunctional metalenses with tailored dispersion properties. (a) Phase at λ_{d1} (490 nm) and λ_{d2} (660 nm) for our library elements and metalens requirements. The blue circles in the left and right panel locate all simulated library elements according to their phase delay. The black dots in the left panel show the target phase at each radial coordinate across Metalens 1 according to Eqs. (2) and (3). For a given black dot (see right panel), any blue circle near the 45° slanted red line can be a candidate that fulfills the phase requirement. This is because for any library element, the Pancharatnam–Berry phase can induce an equal phase shift to all wavelengths. As an example, the purple triangle and green square indicate two library elements that show the same distance to the red line, and their group delays will be compared later to fulfill dispersion requirements. (b) Group delay at λ_{d1} (490 nm) and λ_{d2} (660 nm) for our library elements and metalens requirements. Similar to (a), we located each library element by its group delay, as well as the target group delay, for each coordinate of Metalens 1. The right panel shows that the green square is a better choice than the purple triangle considering the errors (the distance to the black point) of phase and group delay. [(c) and (d)] Phase and group delay fitting for Metalens 1 at the two design wavelengths. The circles show realized values from the selected elements in our library, and the lines show required values. The phase and group delay shown in this figure are relative values. Therefore, they can be negative.

geometric rotation of the nanofins based on the geometric phase, while the group delay is independently tuned by controlling the separation between the nanofins, as well as their length and width.[26,29] The decoupling of these two parameters in our design process allows us to better fulfill the requirements from Eq. (5) compared to isotropic nanostructures.[22,28,31]

RESULTS AND DISCUSSION

Once the design process was in place, we performed simulations to evaluate the metalenses' performance. Metalenses 1 through 3 from Fig. 1(a) were designed with a diameter of 20 μm and a numerical aperture (NA) of 0.2 and 0.1 at wavelengths of 490 nm and 660 nm, respectively. As a first test for each metalens, the amplitude and phase obtained from the library for each individual metalens element was used across the lens surface. This forms a "near-field" wavefront, which was subsequently used to calculate intensity profiles at different planes along the optical axis (point spread function) using the Kirchhoff integration for incident wavelengths from 450 nm to 700 nm. Although the near-field wavefront was approximated by simulating each metalens element with periodic boundary conditions (referred to as unit cell approximation), such an approximation has been shown effective when NA is small.[45,46] It is worth mentioning that although the coupling effect can cause a phase difference in addition to the Pancharatnam–Berry phase for a given nanostructure of different rotations, such an effect has been shown to be small[47] and, to further validate, the supplementary material, Movie 1, shows a full lens FDTD simulation result for an achromatic metalens of 10 μm diameter with performance similar to Metalens 1. The supplementary material provides more simulation details.

The plots of focal length obtained from the Kirchhoff integration are shown in Figs. 3(a)–3(c) as blue circles for designed Metalenses 1–3, while the red lines show designed focal lengths

© Author(s) 2020

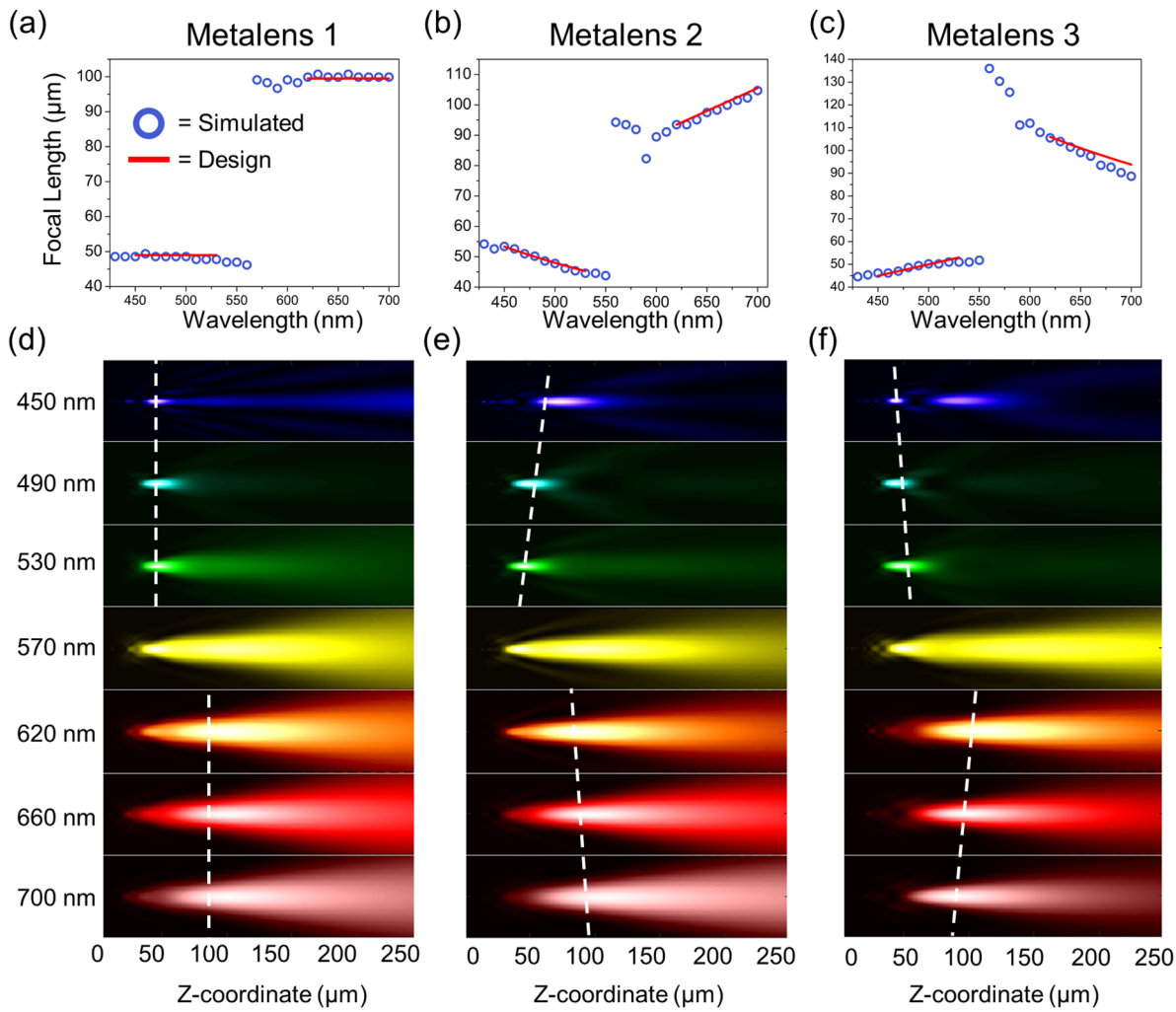

FIG. 3. Simulation results. [(a)–(c)] Focal length shift with respect to wavelength for Metalenses 1–3, respectively. Simulated values are shown as blue circles and designed values as red lines. The focal length is determined by the coordinate of the point that corresponds to the highest intensity along the optical axis. [(d)–(f)] Point spread functions of the right-handed circular polarization component for Metalenses 1–3, respectively, obtained by the Kirchhoff integration. The lenses were placed at z = 0 and illuminated by left-handed circularly polarized light. The white dotted lines guide the eye to the dispersive behavior of each lens. Each point spread function in (d)–(f) corresponds to a metalens shown in (a)–(c).

obtained through Eq. (4). The full point spread functions obtained through the Kirchhoff integration for Metalenses 1–3 are plotted in Figs. 3(d)–3(f), respectively. The dotted lines are plotted to guide the eye to the focal length shift. The agreement between simulated and designed focal length shifts confirms the accuracy of our proposed dispersion engineering method and highlights the versatility of our design, as we can achieve three distinct focal length shifts in varying combinations. The depth of focus (DOF) for λ = 620 –700 nm is longer compared to that of blue and green wavelengths because the NA is lower. In the absence of aberrations and under paraxial approximation (low NA), DOF = $\frac{\lambda}{NA^2}$. We also estimate the efficiency of metalenses from the polarization conversion efficiency of metalens elements, shown in the supplementary material, Fig. S2. Metalens 1 and Metalens 2 show peak efficiencies of approximately 25% around λ = 480 nm. Metalens 3 shows a peak efficiency of 12% at λ = 460 nm. Although the efficiency for these lenses is relatively low, it can be improved by adding an efficiency constraint to only select the high-efficiency elements at the expense of lowering metalens diameter, using taller nanostructures to increase dispersion and polarization conversion efficiency, or by adding new library elements of different shapes than those outlined in Fig. 1(b).[48,49] Additionally, using isotropic elements to design the metalenses could be a solution,[31] although it would likely result in more aberrations.

It is worth mentioning that the lateral size of the focal spots is not identical between the metalenses even though they were

© Author(s) 2020

designed with the same NA at design wavelengths of 490 nm and 660 nm, see the supplementary material, Fig. S3, for an analysis on focal spot sizes and Strehl ratios. This is because of the compromise made in fulfilling the phase and group delay. For example, when looking at the focal spots at the design wavelength 660 nm, Metalens 1 has the largest focal spot and Metalens 3 has the smallest focal spot, implying that Metalens 3 has a better phase fitting at 660 nm. This is to be expected because Metalens 3 displays diffractive dispersion from 620 nm to 700 nm, which requires a much smaller range of group delay. Since the group delay requirements for diffractive behavior are easier to match with our library, there was more freedom to fit the phase at 660 nm for Metalens 3, which resulted in a tighter focal spot and higher Strehl ratio. In Figs. 3(d)–3(f), we also show point spread functions at $\lambda = 570$ nm, which is within the aforementioned bandwidth gap. It can be seen that, in this region, there are two foci, and the shorter one becomes weaker as the incident wavelength increases to 660 nm (also, see supplementary material, Figs. S4–S6, for full point spread functions).

We designed an additional metalens to further showcase the capabilities of our design method. This metalens uses the previous design wavelengths of $\lambda_{d1} = 490$ nm and $\lambda_{d2} = 660$ nm to achromatically focus light with an NA of 0.15 in both bandwidths. For this metalens, however, the designed focal spot profile was a donut from 450 nm to 530 nm and an Airy disk from 620 nm to 700 nm. Figure 4(a) shows the top view of the full lens design. The spiral pattern that can be seen in the metalens layout is due to the azimuthal phase change required to achieve donut focusing. Figure 4(b) plots the realized and required phase profiles at the two design wavelengths along the radial direction. Figure 4(c) shows, at the center wavelength of 490 nm, a clear donut profile that begins to disappear near the edges of the design bandwidth at 450 nm and 530 nm. Similarly, a clear focal spot can be seen at the second design bandwidth of 620–700 nm. This design methodology is also verified by a full lens simulation using Lumerical FDTD, as shown in the supplementary material, Movie 2.

For the metalenses shown here, we consider how the phase for every nanofin varies with wavelength by calculating the group delay. In this way, the metalenses' focal length shift can be controlled over a bandwidth of about 100 nm, while in our previous work of multifunctional metalenses,[22] performance is only maintained for a bandwidth of a few nanometers. These wavelength-multifunctional metalenses,[21–24] also only fulfill phase requirements in design wavelengths and omit the requirement of dispersion, which can result in substantial aberrations for incident wavelengths away from the design wavelengths. The metalenses demonstrated here have small diameters due to their required group delay values in order to control dispersion. The required group delay [first order derivative of Eqs. (2) and (3)] grows rapidly, following a hyperbolic trend. However, the group delay values from our library are limited to about 5 fs for 600-nm-height TiO_2 nanofins. The fact that the nanostructure group delay is capped can be understood by qualitatively treating nanofins as truncated waveguides. Their group delay values are, therefore, given by nanostructure height divided by the group velocity, which is controlled by the group index typically varying between the group index of air and TiO_2. There are many ways to overcome size limitations such as employing multi-layer devices,[24,50,51] high aspect ratio or high index of refraction nanostructures,[52–54] or hybrid metasurface-refractive designs.[35,55,56] Our method, combined

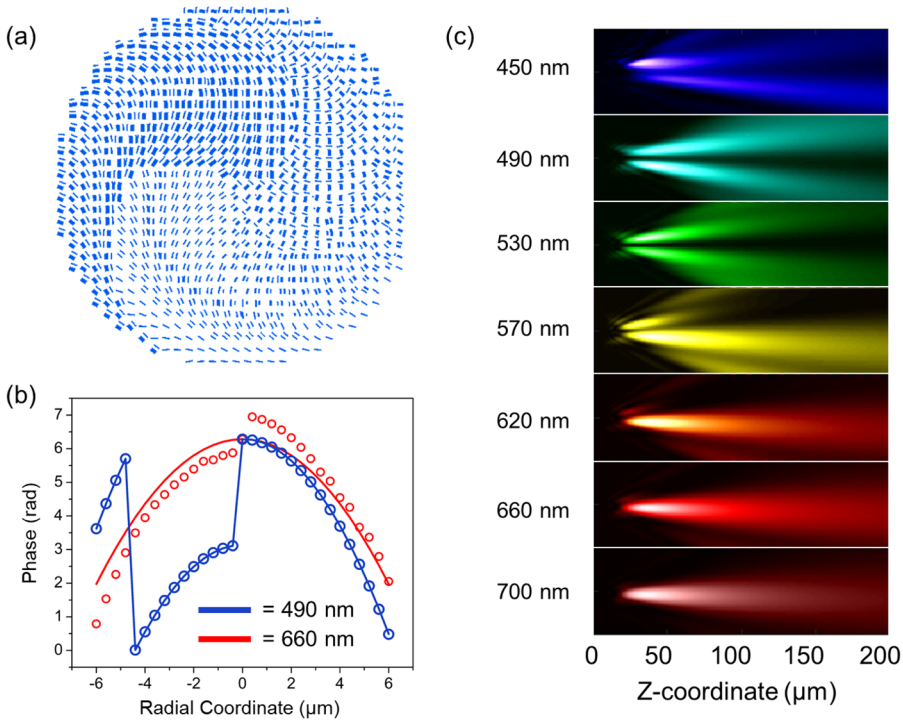

FIG. 4. Design and simulation of a metalens. The metalens focuses blue and red incident wavelengths to a vortex and a spot, respectively. (a) Layout of the metalens with a diameter of 12 μm, NA = 0.15 at $\lambda_{d1} = 490$ nm, and $\lambda_{d2} = 660$ nm. (b) Comparison of the required and realized phases at the two center wavelengths 490 nm and 660 nm. Circles and lines show the phase imparted by the nanofin and the required phase, respectively. Red markings represent the phase at $\lambda_{d2} = 660$ nm, and blue markings represent the phase at $\lambda_{d1} = 490$ nm. (c) Point spread function obtained from the Kirchhoff integration of the layout in (a).

© Author(s) 2020

with a refractive lens in a hybrid system, is particularly promising for reducing aberrations in two well separated bandwidths for two- or three-photon imaging, as well as for stimulated emission depletion (STED) microscopy, without requiring additional phase elements to generate the required donut beam.

CONCLUSIONS

We have shown how dispersion engineering can be used to realize broadband multifunctional metalenses. As examples, we showcased metalenses with dual focal lengths and tailored focal length shifts in two discrete bandwidths in the visible spectrum. In addition, the same design can be applied in beam shaping to achromatically focus an incident plane wave to Airy disk and vortex spots for red and blue wavelengths, respectively. Our lens designs were simulated with an FDTD solver that confirmed the desired performance of our metalenses. The capabilities of our design method open the door to control dispersion in multifunctional metasurfaces for applications such as microscopy and compact optical devices.

SUPPLEMENTARY MATERIAL

See the supplementary material for the analysis on metalens efficiency, focal spot analysis, point spread functions, and a detailed description of our library, as well as supplementary material videos for full-wave simulations of metalenses.

AUTHOR'S CONTRIBUTIONS

J.S. and W.T.C. conceived the study and J.S., A.Y.Z., and W.T.C. performed simulations and developed codes. All authors wrote the manuscript, discussed the results, and commented on the manuscript.

ACKNOWLEDGMENTS

This work was supported by the Defense Advanced Research Projects Agency (Grant No. HR00111810001).

The authors declare no competing interest.

DATA AVAILABILITY

The data that support the findings of this study are available from the corresponding author upon reasonable request.

REFERENCES

[1] N. Yu, P. Genevet, M. A. Kats, F. Aieta, J.-P. Tetienne, F. Capasso, and Z. Gaburro, "Light propagation with phase discontinuities: Generalized laws of reflection and refraction," Science **334**, 333–337 (2011).

[2] A. V. Kildishev, A. Boltasseva, and V. M. Shalaev, "Planar photonics with metasurfaces," Science **339**, 1232009 (2013).

[3] E. Maguid, I. Yulevich, D. Veksler, V. Kleiner, M. L. Brongersma, and E. Hasman, "Photonic spin-controlled multifunctional shared-aperture antenna array," Science **352**, 1202–1206 (2016).

[4] H. Cheng, X. Wei, P. Yu, Z. Li, Z. Liu, J. Li, S. Chen, and J. Tian, "Integrating polarization conversion and nearly perfect absorption with multifunctional metasurfaces," Appl. Phys. Lett. **110**, 171903 (2017).

[5] J. Sung, G. Lee, C. Choi, J. Hong, and B. Lee, "Single-layer bifacial metasurface: Full-space visible light control," Adv. Opt. Mater. **7**, 1801748 (2019).

[6] W. T. Chen, K.-Y. Yang, C.-M. Wang, Y.-W. Huang, G. Sun, I.-D. Chiang, C. Y. Liao, W.-L. Hsu, H. T. Lin, S. Sun, L. Zhou, A. Q. Liu, and D. P. Tsai, "High-efficiency broadband meta-hologram with polarization-controlled dual images," Nano Lett. **14**, 225–230 (2014).

[7] R. Zhao, B. Sain, Q. Wei, C. Tang, X. Li, T. Weiss, L. Huang, Y. Wang, and T. Zentgraf, "Multichannel vectorial holographic display and encryption," Light: Sci. Appl. **7**, 95 (2018).

[8] Z.-L. Deng, J. Deng, X. Zhuang, S. Wang, K. Li, Y. Wang, Y. Chi, X. Ye, J. Xu, G. P. Wang, R. Zhao, X. Wang, Y. Cao, X. Cheng, G. Li, and X. Li, "Diatomic metasurface for vectorial holography," Nano Lett. **18**, 2885–2892 (2018).

[9] D. Wen, S. Chen, F. Yue, K. Chan, M. Chen, M. Ardron, K. F. Li, P. W. H. Wong, K. W. Cheah, E. Y. B. Pun, G. Li, S. Zhang, and X. Chen, "Metasurface device with helicity-dependent functionality," Adv. Opt. Mater. **4**, 321–327 (2016).

[10] A. Arbabi, Y. Horie, M. Bagheri, and A. Faraon, "Dielectric metasurfaces for complete control of phase and polarization with subwavelength spatial resolution and high transmission," Nat. Nanotechnol. **10**, 937–943 (2015).

[11] J. P. Balthasar Mueller, N. A. Rubin, R. C. Devlin, B. Groever, and F. Capasso, "Metasurface polarization optics: Independent phase control of arbitrary orthogonal states of polarization," Phys. Rev. Lett. **118**, 113901 (2017).

[12] Y.-W. Huang, W. T. Chen, W.-Y. Tsai, P. C. Wu, C.-M. Wang, G. Sun, and D. P. Tsai, "Aluminum plasmonic multicolor meta-hologram," Nano Lett. **15**, 3122–3127 (2015).

[13] X. Luo, L. Chen, X. Zhang, Y. Wang, Y. Li, X. Li, Z. Zhao, X. Ma, M. Pu, and M. Hong, "Multicolor 3D meta-holography by broadband plasmonic modulation," Sci. Adv. **2**, e1601102 (2016).

[14] W. Ye, F. Zeuner, X. Li, B. Reineke, S. He, C.-W. Qiu, J. Liu, Y. Wang, S. Zhang, and T. Zentgraf, "Spin and wavelength multiplexed nonlinear metasurface holography," Nat. Commun. **7**, 11930 (2016).

[15] A. S. Backer, "Computational inverse design for cascaded systems of metasurface optics," Opt. Express **27**, 30308 (2019).

[16] Z. L. Deng, J. Deng, X. Zhuang, S. Wang, T. Shi, G. P. Wang, Y. Wang, J. Xu, Y. Cao, X. Wang, X. Cheng, G. Li, and X. Li, "Facile metagrating holograms with broadband and extreme angle tolerance," Light: Sci. Appl. **7**, 78 (2018).

[17] S. M. Kamali, E. Arbabi, A. Arbabi, Y. Horie, M. Faraji-Dana, and A. Faraon, "Angle-multiplexed metasurfaces: Encoding independent wavefronts in a single metasurface under different illumination angles," Phys. Rev. X **7**, 041056 (2017).

[18] W. Liu, Z. Li, H. Cheng, C. Tang, J. Li, S. Zhang, S. Chen, and J. Tian, "Metasurface enabled wide-angle Fourier lens," Adv. Mater. **30**, 1706368 (2018).

[19] A. Akbarzadeh, N. Chamanara, and C. Caloz, "Inverse prism based on temporal discontinuity and spatial dispersion," Opt. Lett. **43**, 3297 (2018).

[20] M. Qiu, M. Jia, S. Ma, S. Sun, Q. He, and L. Zhou, "Angular dispersions in terahertz metasurfaces: Physics and applications," Phys. Rev. Appl. **9**, 054050 (2018).

[21] E. Arbabi, J. Li, R. J. Hutchins, S. M. Kamali, A. Arbabi, Y. Horie, P. Van Dorpe, V. Gradinaru, D. A. Wagenaar, and A. Faraon, "Two-photon microscopy with a double-wavelength metasurface objective lens," Nano Lett. **18**, 4943–4948 (2018).

[22] Z. Shi, M. Khorasaninejad, Y.-W. Huang, C. Roques-Carmes, A. Y. Zhu, W. T. Chen, V. Sanjeev, Z.-W. Ding, M. Tamagnone, K. Chaudhary, R. C. Devlin, C.-W. Qiu, and F. Capasso, "Single-layer metasurface with controllable multiwavelength functions," Nano Lett. **18**, 2420–2427 (2018).

[23] F. Aieta, M. A. Kats, P. Genevet, and F. Capasso, "Multiwavelength achromatic metasurfaces by dispersive phase compensation," Science **347**, 1342–1345 (2015).

[24] Y. Zhou, I. I. Kravchenko, H. Wang, J. R. Nolen, G. Gu, and J. Valentine, "Multilayer noninteracting dielectric metasurfaces for multiwavelength metaoptics," Nano Lett. **18**, 7529–7537 (2018).

[25] M. Ye, V. Ray, and Y. S. Yi, "Achromatic flat subwavelength grating lens over whole visible bandwidths," IEEE Photonics Technol. Lett. **30**, 955–958 (2018).

[26] W. T. Chen, A. Y. Zhu, J. Sisler, Z. Bharwani, and F. Capasso, "A broadband achromatic polarization-insensitive metalens consisting of anisotropic nanostructures," Nat. Commun. **10**, 355 (2019).

[27] W. T. Chen, A. Y. Zhu, V. Sanjeev, M. Khorasaninejad, Z. Shi, E. Lee, and F. Capasso, "A broadband achromatic metalens for focusing and imaging in the visible," Nat. Nanotechnol. **13**, 220–226 (2018).

© Author(s) 2020

[28]E. Arbabi, A. Arbabi, S. M. Kamali, Y. Horie, and A. Faraon, "Controlling the sign of chromatic dispersion in diffractive optics with dielectric metasurfaces," Optica **4**, 625–632 (2017).
[29]R. J. Lin, V.-C. Su, S. Wang, M. K. Chen, T. L. Chung, Y. H. Chen, H. Y. Kuo, J.-W. Chen, J. Chen, Y.-T. Huang, J.-H. Wang, C. H. Chu, P. C. Wu, T. Li, Z. Wang, S. Zhu, and D. P. Tsai, "Achromatic metalens array for full-colour light-field imaging," Nat. Nanotechnol. **14**, 227–231 (2019).
[30]S. Wang, P. C. Wu, V.-C. Su, Y.-C. Lai, M.-K. Chen, H. Y. Kuo, B. H. Chen, Y. H. Chen, T.-T. Huang, J.-H. Wang, R.-M. Lin, C.-H. Kuan, T. Li, Z. Wang, S. Zhu, and D. P. Tsai, "A broadband achromatic metalens in the visible," Nat. Nanotechnol. **13**, 227–232 (2018).
[31]S. Shrestha, A. C. Overvig, M. Lu, A. Stein, and N. Yu, "Broadband achromatic dielectric metalenses," Light: Sci. Appl. **7**, 85 (2018).
[32]M. Khorasaninejad, Z. Shi, A. Y. Zhu, W. T. Chen, V. Sanjeev, A. Zaidi, and F. Capasso, "Achromatic metalens over 60 nm bandwidth in the visible and metalens with reverse chromatic dispersion," Nano Lett. **17**, 1819–1824 (2017).
[33]L. Chen, J. Shakya, and M. Lipson, "Subwavelength confinement in an integrated metal slot waveguide on silicon," Opt. Lett. **31**, 2133 (2006).
[34]L. Tong, J. Lou, and E. Mazur, "Single-mode guiding properties of subwavelength-diameter silica and silicon wire waveguides," Opt. Express **12**, 1025 (2004).
[35]W. T. Chen, A. Y. Zhu, J. Sisler, Y.-W. Huang, K. M. A. Yousef, E. Lee, C.-W. Qiu, and F. Capasso, "Broadband achromatic metasurface-refractive optics," Nano Lett. **18**, 7801–7808 (2018).
[36]A. Y. Zhu, W. T. Chen, J. Sisler, K. M. A. Yousef, E. Lee, Y. W. Huang, C. W. Qiu, and F. Capasso, "Compact aberration-corrected spectrometers in the visible using dispersion-tailored metasurfaces," Adv. Opt. Mater. **7**, 1801144 (2019).
[37]M. Decker, I. Staude, M. Falkner, J. Dominguez, D. N. Neshev, I. Brener, T. Pertsch, and Y. S. Kivshar, "High-efficiency dielectric huygens' surfaces," Adv. Opt. Mater. **3**, 813–820 (2015).
[38]A. I. Kuznetsov, A. E. Miroshnichenko, M. L. Brongersma, Y. S. Kivshar, and B. Luk'yanchuk, "Optically resonant dielectric nanostructures," Science **354**, aag2472 (2016).
[39]S. S. Wang and R. Magnusson, "Theory and applications of guided-mode resonance filters," Appl. Opt. **32**, 2606 (1993).
[40]A. C. Overvig, S. Shrestha, and N. Yu, "Dimerized high contrast gratings," Nanophotonics **7**, 1157–1168 (2018).
[41]P. Lalanne, "Waveguiding in blazed-binary diffractive elements," J. Opt. Soc. Am. A **16**, 2517 (1999).
[42]R. C. Devlin, M. Khorasaninejad, W. T. Chen, J. Oh, and F. Capasso, "Broadband high-efficiency dielectric metasurfaces for the visible spectrum," Proc. Natl. Acad. Sci. U. S. A. **113**, 10473–10478 (2016).
[43]S. Pancharatnam, "Generalized theory of interference and its applications," Proc. - Indian Acad. Sci., Sect. A **44**, 398–417 (1956).
[44]M. V. Berry, "The adiabatic phase and Pancharatnam's phase for polarized light," J. Mod. Opt. **34**, 1401–1407 (1987).
[45]Z. Lin, V. Liu, R. Pestourie, and S. G. Johnson, "Topology optimization of freeform large-area metasurfaces," Opt. Express **27**, 15765 (2019).
[46]H. Chung and O. D. Miller, "High-NA achromatic metalenses by inverse design," Opt. Express **28**, 6945–6965 (2019).
[47]G. Zheng, H. Mühlenbernd, M. Kenney, G. Li, T. Zentgraf, and S. Zhang, "Metasurface holograms reaching 80% efficiency," Nat. Nanotechnol. **10**, 308–312 (2015).
[48]M. Pu, X. Li, X. Ma, Y. Wang, Z. Zhao, C. Wang, C. Hu, P. Gao, C. Huang, H. Ren, X. Li, F. Qin, J. Yang, M. Gu, M. Hong, and X. Luo, "Catenary optics for achromatic generation of perfect optical angular momentum," Sci. Adv. **1**, e1500396 (2015).
[49]H. Kikuta, Y. Ohira, and K. Iwata, "Achromatic quarter-wave plates using the dispersion of form birefringence," Appl. Opt. **36**, 1566 (1997).
[50]B. Groever, W. T. Chen, and F. Capasso, "Meta-lens doublet in the visible region," Nano Lett. **17**, 4902–4907 (2017).
[51]A. Arbabi, E. Arbabi, S. M. Kamali, Y. Horie, S. Han, and A. Faraon, "Miniature optical planar camera based on a wide-angle metasurface doublet corrected for monochromatic aberrations," Nat. Commun. **7**, 13682 (2016).
[52]E. Shkondin, O. Takayama, J. M. Lindhard, P. V. Larsen, M. D. Mar, F. Jensen, and A. V. Lavrinenko, "Fabrication of high aspect ratio TiO_2 and Al_2O_3 nanogratings by atomic layer deposition," J. Vac. Sci. Technol., A **34**, 031605 (2016).
[53]S. Gorelick, V. A. Guzenko, J. Vila-Comamala, and C. David, "Direct *e*-beam writing of dense and high aspect ratio nanostructures in thick layers of PMMA for electroplating," Nanotechnology **21**, 295303 (2010).
[54]D. Sell, J. Yang, S. Doshay, K. Zhang, and J. A. Fan, "Visible light metasurfaces based on single-crystal silicon," ACS Photonics **3**, 1919–1925 (2016).
[55]R. Sawant, P. Bhumkar, A. Y. Zhu, P. Ni, F. Capasso, and P. Genevet, "Mitigating chromatic dispersion with hybrid optical metasurfaces," Adv. Mater. **31**, 1805555 (2019).
[56]J. Nagar, S. D. Campbell, and D. H. Werner, "Apochromatic singlets enabled by metasurface-augmented GRIN lenses," Optica **5**, 99 (2018).

© Author(s) 2020